ELSEVIER

Journal of Fluids and Structures 24 (2008) 819–832

JOURNAL OF FLUIDS AND STRUCTURES

www.elsevier.com/locate/jfs

Grid movement techniques and their influence on laminar fluid–structure interaction computations

S. Yigit*, M. Schäfer, M. Heck

Department of Numerical Methods in Mechanical Engineering, Technische Universität Darmstadt, Petersenstr. 30, 64287 Darmstadt, Germany

Received 8 February 2007; accepted 1 December 2007
Available online 18 April 2008

Abstract

The efficiency and accuracy of grid movement methods for a typical fluid–structure interaction configuration is investigated. The set-up consists of a thin elastic structure including one rotational degree of freedom fixed in a laminar channel flow. Two different cases are considered, i.e., small and large structural deformations. The comparison is carried out by using two algebraic methods, linear and transfinite interpolation, and two elliptic solution strategies also providing boundary orthogonality. A reference solution is obtained from a mixed approach. The evaluation of efficiency and accuracy is based on computation times, number of coupling steps, structural displacements and swiveling frequencies. All mesh movement techniques are employed in the frame of a partitioned solution procedure involving the block-structured finite-volume flow solver FASTEST, the finite-element structural solver FEAP, and the coupling interface MpCCI.

Keywords: Elliptic; FSI; Grid generation; Large deformations

1. Introduction

The choice of an appropriate grid movement concept for fluid–structure interaction computations depends on many different aspects. Not only the efficiency of the grid generation process for itself has to be taken into account, but also the required coupling strategy to cope with the investigated physical phenomenon.

Coupled fluid–solid problems can be divided into different categories. Either the mesh topology changes during the computation (e.g., additional interaction of solid walls) or it remains unchanged. While in the first case a totally new re-meshing is required, the second case allows for a choice between different existing grid movement strategies. Applications with topology changes have been barely investigated yet, but there exist several grid movement methods for the second case which will be investigated in this work.

In the articles of Löhner and Yang (1996) and Longatte et al. (2003) modified Laplacian operators are used for non-structured grids with special treatment of near wall regions involving parameters for distance estimation. Albert and O'Neill (1986) employed a transfinite mapping strategy with bilinear and trilinear projectors for phase change analysis. The spring analogy is another technique often used. Here, the mesh nodes are connected through different kinds of

*Corresponding author. Tel.: +49 6151 16 2384.
E-mail address: yigit@fnb.tu-darmstadt.de (S. Yigit).

0889-9746/$ - see front matter © 2007 Elsevier Ltd. All rights reserved.
doi:10.1016/j.jfluidstructs.2007.12.002

springs, mostly linear. Farhat et al. (1998) applied longitudinal and torsional springs and Murayama et al. (2002) included also special wall treatment. In the linear elasticity approach the spatial fluid domain is assumed to be an elastic continuum. Stein et al. (2003) employed this method incorporating a re-meshing algorithm for unstructured grids and large deformations. Baker (2001) also used re-meshing. In Bar-Yoseph et al. (2001) the fluid mesh is considered as a pseudo-non-linear elastostatic problem applied to structured and unstructured grids.

Many of the mentioned algorithms can be applied to structured and unstructured grids within a partitioned solution procedure. In case of monolithic solution strategies, solving the coupled problem simultaneously, an iterative grid smoothing method will further complicate the numerical solution process. Generally speaking, the more accurate and universally applicable the method, the more complex and time-consuming is the computation and implementation. Systematic comparisons of grid movement techniques, like the spring analogy and linear elasticity, are given in Yang and Mavriplis (2005).

In the present paper we consider approaches for the special case of block-structured grids. In contrast to unstructured grids (often using advancing-front, octree or Delaunay-based methods), the mesh topology has to be kept unchanged within one structured block. As further demands, boundary grid points should not move along edges and the whole mesh has to be capable of large deformations without grid folding and extreme cell distortions. We systematically compare several algebraic and elliptic methods show their advantages and disadvantages according to accuracy, robustness and computation times for the flow solver and mesh generation procedure.

2. Governing equations

We consider a problem domain Ω consisting of a fluid part Ω_f and a solid part Ω_s. For the fluid domain part Ω_f, we assume a flow of an incompressible Newtonian fluid. In this case the basic conservation equations governing transport of mass and momentum for a fluid control volume V_f with surface S_f are given by

$$\int_{S_f} (\boldsymbol{v} - \boldsymbol{v}^g) \cdot \boldsymbol{n} \, \mathrm{d}S_f = 0, \tag{1}$$

$$\frac{\partial}{\partial t} \int_{V_f} \rho_f \boldsymbol{v} \, \mathrm{d}V_f + \int_{S_f} \rho_f (\boldsymbol{v} - \boldsymbol{v}^g)(\boldsymbol{v} \cdot \boldsymbol{n}) \, \mathrm{d}S_f = \int_{V_f} \rho_f \boldsymbol{f}_f \, \mathrm{d}V_f + \int_{S_f} \boldsymbol{T}_f \cdot \boldsymbol{n} \, \mathrm{d}S_f, \tag{2}$$

where $\boldsymbol{v}$ is the velocity vector with respect to Cartesian coordinates $\boldsymbol{x}$, t is the time, ρ_f is the fluid density, $\boldsymbol{n}$ is the outward normal vector and $\boldsymbol{f}_f$ are external volume forces (e.g., buoyancy forces); $\boldsymbol{v}^g$ is the velocity with which S_f may move (grid velocity) due to displacements of solid parts. The Cauchy stress tensor $\boldsymbol{T}_f$ for incompressible Newtonian fluids is defined by

$$\boldsymbol{T}_f = \mu_f (\nabla \boldsymbol{v} + \nabla \boldsymbol{v}^{\mathrm{T}}) - p \boldsymbol{I}, \tag{3}$$

with the pressure p, the dynamic viscosity μ_f, the vector gradient ∇ and the identity tensor $\boldsymbol{I}$.

For the structure we denote a material point in the reference configuration as $\boldsymbol{X}$ whose position in the current configuration is given by

$$\boldsymbol{x} = \boldsymbol{\chi}(\boldsymbol{X}, t). \tag{4}$$

The displacements are evaluated by

$$\boldsymbol{u} = \boldsymbol{x} - \boldsymbol{X}. \tag{5}$$

For more details see Truesdell and Noll (2004) and Ogden (1997). The basic balance equation for momentum for the solid domain Ω_s can be written as

$$\nabla \cdot (\boldsymbol{F}_s \boldsymbol{S}_s^{\mathrm{T}}) + \rho_s \boldsymbol{f}_s = \rho_s \ddot{\boldsymbol{\chi}}, \tag{6}$$

where $\ddot{\boldsymbol{\chi}} = \partial^2 \boldsymbol{\chi}(\boldsymbol{X}, t)/\partial t^2$ is the acceleration, $\boldsymbol{S}_s$ denotes the second Piola–Kirchhoff stress tensor, ρ_s is the density of the solid, and $\boldsymbol{f}_s$ are external volume forces acting on the solid (e.g., gravitational forces). $\boldsymbol{F}_s = \partial \boldsymbol{\chi}/\partial \boldsymbol{X}$ denotes the deformation gradient.

In the present investigation we consider the Saint Venant–Kirchhoff material law

$$\boldsymbol{S}_s = \lambda_s \, \mathrm{tr} \boldsymbol{E} \, \boldsymbol{I} + 2\mu_s \boldsymbol{E}, \tag{7}$$

with the Green–Lagrangian strain tensor

$$\boldsymbol{E} = \tfrac{1}{2}(\boldsymbol{F}_s^{\mathrm{T}} \boldsymbol{F}_s - \boldsymbol{I}) \tag{8}$$

as kinematic property. λ_s and μ_s are the two Lamé constants that can also be expressed with Young's modulus E_s and Poisson ratio v_s by

$$E_s = \frac{\mu_s(3\lambda_s + 2\mu_s)}{\lambda_s + \mu_s} \quad \text{and} \quad v_s = \frac{\lambda_s}{2(\lambda_s + \mu_s)}. \tag{9}$$

The problem formulation has to be closed by prescribing suitable boundary and interface conditions. On solid and fluid boundaries Γ_s and Γ_f, standard conditions as for individual solid and fluid problems can be prescribed. For the velocities and the stresses on a fluid–solid interface Γ_i, we have the conditions

$$\boldsymbol{v} = \dot{\boldsymbol{\chi}} = \boldsymbol{v}_\mathrm{b} \quad \text{and} \quad \boldsymbol{T}_f \boldsymbol{n} = \boldsymbol{T}_s \boldsymbol{n}, \tag{10}$$

where $\boldsymbol{v}_\mathrm{b}$ is the velocity of the interface and $\boldsymbol{T}_s = \boldsymbol{F}_s \boldsymbol{S}_s \boldsymbol{F}_s^\mathrm{T} / \det \boldsymbol{F}_s$ is the Cauchy stress tensor.

3. Numerical fluid–structure coupling scheme

The discretization of the problem domain is based on a block-structuring technique. Fluid and solid parts are assigned to different blocks. Solid blocks are treated by the finite-element solver FEAP, see Taylor (2002). For the fluid blocks, which can be defined as moving or fixed, the parallel multigrid finite-volume flow solver FASTEST is employed, see Schäfer et al. (2001). Both solvers involve second-order spatial discretizations and fully implicit second-order time discretizations.

For the fluid–structure coupling, an implicit partitioned approach is employed. In Fig. 1 a schematic view of the iteration process is given. After the initializations, the flow field is determined in the actual flow geometry. From this, the friction and pressure forces on the interacting walls are computed. These are passed to the structural solver as boundary conditions (it is used a conservative interpolation method with four weights for each quadrilateral coupled element; see Fraunhofer SCAI, 2004). The structural solver computes the deformations (interpolations of displacements are non-conservative; see Fraunhofer SCAI, 2004), with which then the fluid mesh is modified by one of the mentioned grid movement techniques. Afterwards the flow solver is started again. For the arbitrary Lagrangian–Eulerian description, see Donea et al. (2004), a discrete form of the space conservation law

$$\frac{\mathrm{d}}{\mathrm{d}t} \int_{V_f} \mathrm{d}V = \int_{S_f} \boldsymbol{v}^\mathrm{g} \boldsymbol{n} \, \mathrm{d}S \tag{11}$$

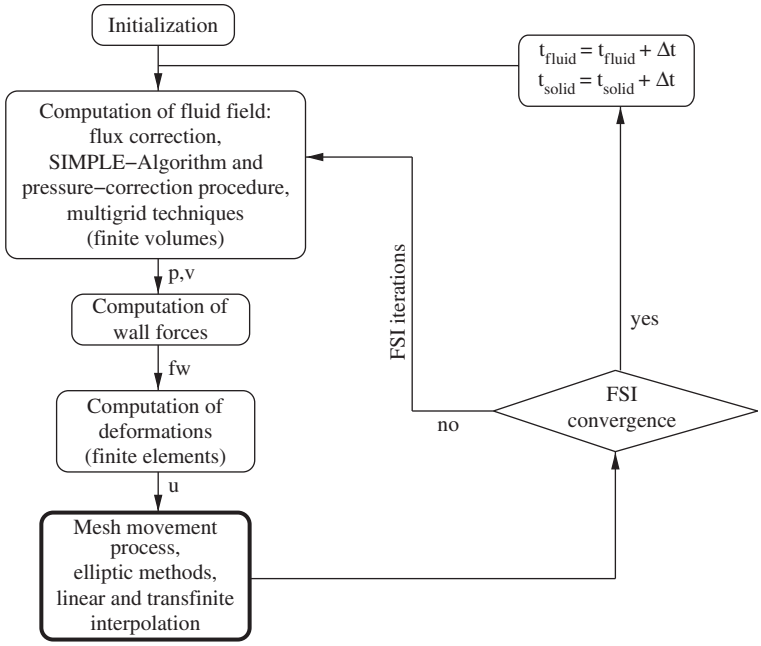

Fig. 1. Flow chart of coupled solution procedure.

is taken into account in order to compute the additional convective fluxes in (1) and (2) for blocks that are moving. This is done via the swept volumes δV_c of the control volume faces for which one has the relation (Demirdžić and Perić, 1988):

$$\sum_c \frac{\delta V_c^n}{\Delta t_n} = \frac{V_f^n - V_f^{n-1}}{\Delta t_n} = \sum_c (\boldsymbol{v}^g \boldsymbol{n} S_f)_c^n, \tag{12}$$

where the summation index c runs over the faces of the control volume, the index n denotes the time level t_n and Δt_n is the time step size. By this way interface displacements enter the fluid problem part in a manner strictly ensuring mass conservation.

The fluid–structure interaction iteration loop is repeated until a convergence criterion $\varepsilon_{\mathrm{FSI}}$ is reached, which is defined by the change of the mean displacements

$$\frac{1}{N}\sum_{k=1}^{N} \frac{\|\boldsymbol{u}^{k,m-1} - \boldsymbol{u}^{k,m}\|_\infty}{\|\boldsymbol{u}^{k,m}\|_\infty} < \varepsilon_{\mathrm{FSI}}, \tag{13}$$

where m is the FSI iteration counter, N is the number of interface nodes, and $\|\cdot\|_\infty$ denotes the infinite norm. Note that an explicit coupling method would be obtained, if only one FSI iteration is performed.

The data transfer between the flow and solid solvers within the partitioned solution procedure is performed via an interface realized by the coupling library MpCCI [see Fraunhofer SCAI (2004)] that controls the data communication and also carries out the interpolations of the data from the fluid and solid grids. More details are given in Schäfer et al. (2006).

Various test computations have shown that the coupling scheme is rather sensitive with respect to the deformations in the first FSI iterations. Here, situations that are far away from the physical equilibrium can arise, which may lead to instabilities or even the divergence of the FSI iterations. In order to counteract this effect an underrelaxation is employed. The actually computed displacements $\boldsymbol{u}^{\mathrm{act}}$ are (linearly) weighted with the values $\boldsymbol{u}^{\mathrm{old}}$ from the preceding iteration to give the new displacements $\boldsymbol{u}^{\mathrm{new}}$:

$$\boldsymbol{u}^{\mathrm{new}} = \alpha_{\mathrm{FSI}} \boldsymbol{u}^{\mathrm{act}} + (1 - \alpha_{\mathrm{FSI}}) \boldsymbol{u}^{\mathrm{old}}, \tag{14}$$

where $0 < \alpha_{\mathrm{FSI}} \leqslant 1$. Note that the underrelaxation does not change the final converged result.

4. Grid movement techniques

The method for moving the grid in the fluid domain constitutes an important component of the coupled solution procedure, in particular in the case of larger structural deformations. Besides the requirements that no grid folding occurs and that the mesh exactly fits the moving boundaries one has to take care that distortions of control volumes are kept to a minimum in order not to deteriorate the discretization accuracy and the efficiency of the solver.

We consider algebraic and elliptic mesh generation techniques for the grid movement involving either boundary orthogonality or grid spacing control. Additionally, a mixed approach combines both capabilities. To simplify the presentation we describe the approaches for a single two-dimensional (2-D) structured block surrounded by four boundary curves I–IV (see Fig. 2). The generalization to the three-dimensional (3-D) case and to multiple blocks is straightforward.

For a structured 2-D block, there is a one-to-one mapping $\boldsymbol{x}(\xi,\eta) = (x(\xi,\eta), y(\xi,\eta))$ of the physical coordinates $\boldsymbol{x} = (x, y)$ to computational coordinates (ξ, η) where, without loss of generality, $0 \leqslant \xi \leqslant 1$ and $0 \leqslant \eta \leqslant 1$. In each FSI iteration the coordinates of the interior grid points have to be computed from the given boundary point distribution.

First, we consider algebraic approaches. A very simple method is obtained by linear interpolation between opposite boundaries, e.g., boundary I–III. Let the distances between neighbouring grid points be

$$d_{i,j} = \|\boldsymbol{x}_{i,j} - \boldsymbol{x}_{i-1,j}\|, \quad i = 1 \ldots N, \; j = 0 \ldots M, \tag{15}$$

with the overall lengths

$$L_j = \sum_{i=1}^{N} d_{i,j}, \quad j = 0 \ldots M. \tag{16}$$

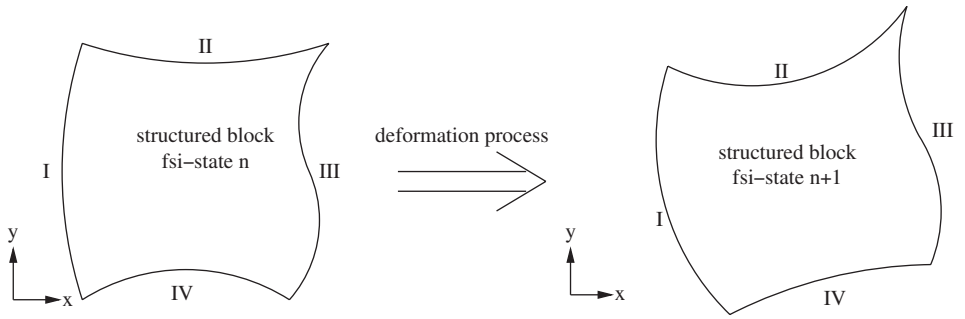

Fig. 2. Deformation of structured two-dimensional block.

The normalized lengths for the parametrization are

$$\bar{L}_{i,j} = \frac{1}{L_j}\sum_{m=1}^{i} d_{m,j}, \quad i = 1 \ldots N, \; j = 0 \ldots M, \quad \bar{L}_{0,j} = 0. \tag{17}$$

The grid point coordinates in the domain are then computed by

$$\boldsymbol{x}_{i,j} = (\boldsymbol{x}_{N,j} - \boldsymbol{x}_{0,j}) \cdot \bar{L}_{i,j} + \boldsymbol{x}_{0,j}, \quad i = 0 \ldots N, \; j = 0 \ldots M. \tag{18}$$

Another algebraic method is the linear transfinite interpolation (TFI), where the interior grid points are computed by

$$\begin{aligned}\boldsymbol{x}(\xi,\eta) = {} & (1-\eta)\boldsymbol{x}(\xi,0) + \eta\boldsymbol{x}(\xi,1) + (1-\xi)\boldsymbol{x}(0,\eta) + \xi\boldsymbol{x}(1,\eta) - \xi[\eta\boldsymbol{x}(1,1) + (1-\eta)\boldsymbol{x}(1,0)] \\ & - (1-\xi)[\eta\boldsymbol{x}(0,1) + (1-\eta)\boldsymbol{x}(0,0)].\end{aligned} \tag{19}$$

For boundary movement a very efficient and simple algebraic method is employed. The cubic polynomial interpolation with normalized parameter $\bar{L}$, see Eq. (17), combines two given boundary points $\boldsymbol{x}(\bar{L}=0)$ and $\boldsymbol{x}(\bar{L}=1)$ and also involves their corresponding tangents $\boldsymbol{x}_t(\bar{L}=0)$ and $\boldsymbol{x}_t(\bar{L}=1)$:

$$\boldsymbol{x}(\bar{L}) = \boldsymbol{a}_3\bar{L}^3 + \boldsymbol{a}_2\bar{L}^2 + \boldsymbol{a}_1\bar{L} + \boldsymbol{a}_0, \quad 0 \leqslant \bar{L} \leqslant 1, \tag{20}$$

with the coefficients

$$\boldsymbol{a}_3 = 2\boldsymbol{x}(0) - 2\boldsymbol{x}(1) + \boldsymbol{x}_t(0) + \boldsymbol{x}_t(1), \quad \boldsymbol{a}_2 = -3\boldsymbol{x}(0) + 3\boldsymbol{x}(1) - 2\boldsymbol{x}_t(0) - \boldsymbol{x}_t(1), \tag{21,22}$$

$$\boldsymbol{a}_1 = \boldsymbol{x}_t(0), \quad \boldsymbol{a}_0 = \boldsymbol{x}(0). \tag{23,24}$$

The tangents $\boldsymbol{x}_t$ are chosen to be perpendicular to boundary surfaces.

We now turn our attention to the elliptic methods. We adopt an approach described in Spekreijse (1995) which is based on the following (elliptic) Poisson equation for the physical coordinates:

$$a\boldsymbol{x}_{\xi\xi} - 2b\boldsymbol{x}_{\xi\eta} + c\boldsymbol{x}_{\eta\eta} + (aP_{11}^1 - 2bP_{12}^1 + cP_{13}^1)\boldsymbol{x}_\xi + (aP_{11}^2 - 2bP_{12}^2 + cP_{13}^2)\boldsymbol{x}_\eta = \boldsymbol{0}, \tag{25}$$

with the control functions

$$\boldsymbol{P}_{11} = \frac{1}{s_\eta t_\xi - s_\xi t_\eta}\begin{bmatrix} t_\eta & -s_\eta \\ -t_\xi & s_\xi \end{bmatrix}\begin{Bmatrix} s_{\xi\xi} \\ t_{\xi\xi} \end{Bmatrix}, \tag{26}$$

$$\boldsymbol{P}_{12} = \frac{1}{s_\eta t_\xi - s_\xi t_\eta}\begin{bmatrix} t_\eta & -s_\eta \\ -t_\xi & s_\xi \end{bmatrix}\begin{Bmatrix} s_{\xi\eta} \\ t_{\xi\eta} \end{Bmatrix}, \tag{27}$$

$$\boldsymbol{P}_{13} = \frac{1}{s_\eta t_\xi - s_\xi t_\eta}\begin{bmatrix} t_\eta & -s_\eta \\ -t_\xi & s_\xi \end{bmatrix}\begin{Bmatrix} s_{\eta\eta} \\ t_{\eta\eta} \end{Bmatrix}, \tag{28}$$

and the abbreviations

$$a = x_\eta x_\eta + y_\eta y_\eta, \quad b = x_\xi x_\eta + y_\xi y_\eta, \quad c = x_\xi x_\xi + y_\xi y_\xi. \tag{29}$$

The indices ξ and η denote the corresponding derivatives. Fig. 3 shows how the mapping between the computational space and the physical domain is performed through the parameter space (s,t) that can be used to control the quality of the mesh.

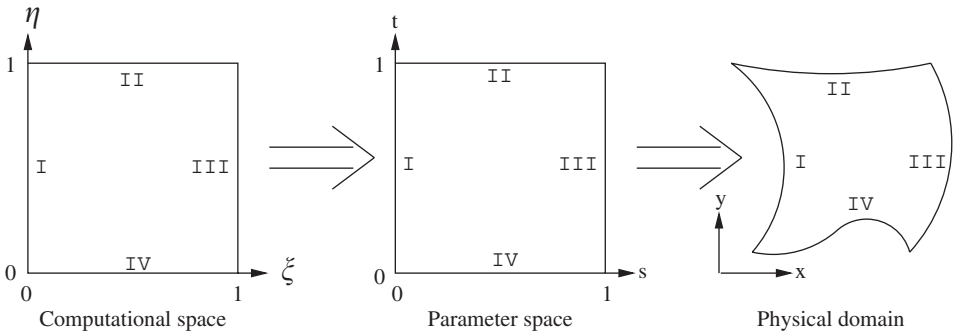

Fig. 3. Mapping strategy for elliptic grid movement.

We consider a parameter space with $s(\mathrm{I}) = 0$, $s(\mathrm{III}) = 1$, $t(\mathrm{IV}) = 0$, and $t(\mathrm{II}) = 1$. The point distribution along $s(\mathrm{II})$, $s(\mathrm{IV})$, $t(\mathrm{I})$, and $t(\mathrm{III})$ arises from linear interpolation along these boundaries involving the normalized arc length. The inner parameter domain is adapted by solving simultaneously:

$$s = s(\mathrm{IV})(1-t) + s(\mathrm{II})t, \tag{30}$$

$$t = t(\mathrm{I})(1-s) + t(\mathrm{III})s. \tag{31}$$

Next, the control functions P^i_{11}, P^i_{12}, P^i_{13}, $i = 1, 2$ can be computed according to Eqs. (26)–(28) and remain unchanged during the solution of (25). The derivatives in Eq. (25) are approximated by central differences (CDS) and a Picard iteration process is used for linearization:

$$a^{k-1}\boldsymbol{x}^k_{\xi\xi} - 2b^{k-1}\boldsymbol{x}^k_{\xi\eta} + c^{k-1}\boldsymbol{x}^k_{\eta\eta} + (a^{k-1}P^1_{11} - 2b^{k-1}P^1_{12} + c^{k-1}P^1_{13})\boldsymbol{x}^k_{\xi} + (a^{k-1}P^2_{11} - 2b^{k-1}P^2_{12} + c^{k-1}P^2_{13})\boldsymbol{x}^k_{\eta} = \boldsymbol{0}. \tag{32}$$

In each step this equation system is solved by the Gauß–Seidel algorithm for the unknown grid coordinates $x^k_{i,j}$ and $y^k_{i,j}$, $i = 1 \ldots N-1$, $j = 1 \ldots M-1$. The Picard iteration process is repeated as long as the convergence criterion $\varepsilon_{\mathrm{GRID}}$ is satisfied:

$$\frac{\sum_{i=0}^{N}\sum_{j=0}^{M}\|\boldsymbol{x}^{\mathrm{act}}_{i,j} - \boldsymbol{x}^{\mathrm{old}}_{i,j}\|_\infty}{\sum_{i=0}^{N}\|\boldsymbol{x}^{\mathrm{act}}_{i,0} - \boldsymbol{x}^{\mathrm{act}}_{i,M}\|_\infty \cdot \sum_{j=0}^{M}\|\boldsymbol{x}^{\mathrm{act}}_{0,j} - \boldsymbol{x}^{\mathrm{act}}_{N,j}\|_\infty} < \varepsilon_{\mathrm{GRID}}. \tag{33}$$

Within the FSI iteration process the coordinates of the previous iteration are applied as initial values. The whole solution algorithm, which is summarized schematically in Fig. 4, operates like a mesh smoother. In any case a boundary conforming mesh without grid folding results for which the interior grid point distribution is a good reflection of the prescribed boundary grid point distribution.

The method described can be extended according to Spekreijse (1995) with respect to boundary orthogonality. First, a boundary conforming grid without grid folding is computed applying the elliptic method explained above. For this mesh, we consider the Laplace equations:

$$\Delta s = \frac{\partial^2 s}{\partial x^2} + \frac{\partial^2 s}{\partial y^2} = \left(\frac{1}{J}as_\xi - \frac{1}{J}bs_\eta\right)_\xi + \left(-\frac{1}{J}bs_\xi + \frac{1}{J}cs_\eta\right)_\eta = 0, \tag{34}$$

$$\Delta t = \frac{\partial^2 t}{\partial x^2} + \frac{\partial^2 t}{\partial y^2} = \left(\frac{1}{J}at_\xi - \frac{1}{J}bt_\eta\right)_\xi + \left(-\frac{1}{J}bt_\xi + \frac{1}{J}ct_\eta\right)_\eta = 0, \tag{35}$$

with the abbreviations

$$a = x_\eta x_\eta + y_\eta y_\eta, \quad b = x_\xi x_\eta + y_\xi y_\eta, \quad c = x_\xi x_\xi + y_\xi y_\xi, \quad J = x_\xi y_\eta - x_\eta y_\xi$$

in combination with the Neumann boundary conditions

$$\frac{\partial s}{\partial \boldsymbol{n}} = 0, \quad \frac{\partial t}{\partial \boldsymbol{n}} = 0, \tag{36}$$

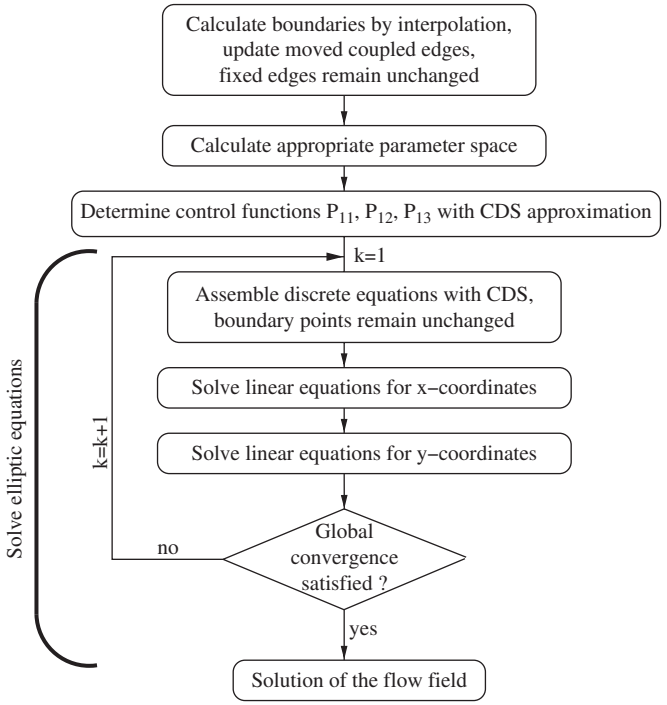

Fig. 4. Flow chart of the elliptic mesh movement method.

where $\boldsymbol{n} = (n_1, n_2)$ is the outward unit normal vector. Eqs. (34) and (35) involve a divergence expression that allows for applying the finite-volume method:

$$\int_\Omega \left[\frac{1}{J}(as_\xi - bs_\eta)\right]_\xi + \left[\frac{1}{J}(-bs_\xi + cs_\eta)\right]_\eta \mathrm{d}\xi\,\mathrm{d}\eta = \int_{\partial\Omega}\left[\frac{1}{J}(s_\xi(an_1 - bn_2) + s_\eta(-bn_1 + cn_2))\right]\mathrm{d}\sigma = 0, \tag{37}$$

$$\int_\Omega \left[\frac{1}{J}(at_\xi - bt_\eta)\right]_\xi + \left[\frac{1}{J}(-bt_\xi + ct_\eta)\right]_\eta \mathrm{d}\xi\,\mathrm{d}\eta = \int_{\partial\Omega}\left[\frac{1}{J}(t_\xi(an_1 - bn_2) + t_\eta(-bn_1 + cn_2))\right]\mathrm{d}\sigma = 0, \tag{38}$$

where the integration is done for a control volume Ω and its boundary $\partial\Omega$ with the line element $\mathrm{d}\sigma$, respectively. The computational domain is discretized by unit control volumes for inner points and half control volumes for boundary points, leading to one system of linear equations for s and t, respectively. Since the boundary conditions (36) transform to

$$\frac{1}{J}(s_\xi(an_1 - bn_2) + s_\eta(-bn_1 + cn_2)) = 0, \tag{39}$$

$$\frac{1}{J}(t_\xi(an_1 - bn_2) + t_\eta(-bn_1 + cn_2)) = 0, \tag{40}$$

these terms have to be set to zero for the desired orthogonal grid lines at boundaries. During the solution procedure, boundary points are moved along edges (s(IV), s(II)) until convergence is reached. These points are combined by cubic Hermite interpolation:

$$s = s(\mathrm{IV})(1+2t)(1-t)^2 + s(\mathrm{II})(3-2t)t^2, \quad 0 \leqslant t \leqslant 1, \tag{41}$$

$$t = t(\mathrm{I})(1+2s)(1-s)^2 + t(\mathrm{III})(3-2s)s^2, \quad 0 \leqslant s \leqslant 1. \tag{42}$$

Since the interpolation is given analytically, the Jacobian matrix and its inverse can easily be calculated and solved simultaneously for s and t by the Newton algorithm. As initial condition the parameter space values from the first elliptic solution are applied, leading to convergence after one or two Newton iterations.

This way we have obtained a new parameter space to compute the desired control functions for boundary orthogonalization. Finally, the desired grid is computed by solving the elliptic equations once again. The main steps of

the elliptic-orthogonal method can be summarized as follows:

(i) calculate boundaries by interpolation, update moved coupled edges, fixed edges remain unchanged;
(ii) calculate parameter space by normalized arc length;
(iii) determine control functions P_{11}, P_{12}, P_{13} with CDS approximation;
(iv) solve elliptic equations, according to Fig. 4;
(v) solve Laplace equations for s and t to get new boundary point distribution;
(vi) perform cubic Hermite interpolation for s and t by Newton's method;
(vii) determine control functions P_{11}, P_{12}, P_{13} with CDS approximation;
(viii) solve elliptic equations once again, according to Fig. 4.

The advantages of this approach lie in the great flexibility allowing independent orthogonalization of all four boundaries while keeping the edge point distribution unchanged. Furthermore, the method is very robust and may even work in case of rather large deformations.

5. Test configuration and simulation parameters

Fig. 5 shows the test configuration including an elastic structure and the fluid domain decomposition into structured blocks (blocks 1 and 10 are fixed, blocks 2–9 are able to move). The fluid with density $\rho_f = 1000\,\mathrm{kg/m^3}$ and dynamic viscosity $\mu_f = 0.5375\,\mathrm{kg/ms}$ enters the channel uniformly with 2 m/s. The structural configuration is presented in Fig. 6. It is divided into two regions with different material properties. The transition from small to large deformations is carried out by decreasing Young's modulus of the rear part. The kinematic motion consists of a superimposition of free rotation around the point of origin and elastic deformations.

The structure is discretized by 500 linear solid hexahedrons with an enhanced strain formulation to prevent locking effects, see Taylor (2003). For the fluid domain four refinement levels are considered, i.e., 1120, 4480, 17 920 and 71 680 control volumes (discretization levels 1 to 4) for all grid movement techniques and all deformations. The finest mesh, 286 720 control volumes (discretization level 5), is used for reference purpose. The time step size is 0.002 s and α_{FSI} is 0.5 for all computations. The fluid field properties are solved up to a convergence criterion of 1×10^{-4}. The residual normalization is performed by summing up all residuals and dividing by the overall incoming flux.

Fig. 7 illustrates the concept of boundary movement. First, the structural displacements are updated for the coupled surfaces. Afterwards the block edges are interpolated between the coupling areas and the fixed domains. Finally, the inner parts are adopted by smoothing techniques or interpolation.

For the reference case (I), blocks five and six are divided into two regions. For region (b), a linear interpolation is employed along orthogonal lines obtaining complete boundary control, i.e., exact orthogonality combined with exact grid spacing determination. Region (a) and all other blocks are smoothed by the elliptic method, except blocks 3 and 8 which occupy only a very thin strip for which cubic polynomial interpolation can be applied.

For the elliptic, orthogonal and TFI methods (II) the blocks are generated by corresponding techniques. The boundary discretizations are equal for all three cases. The method (III) interpolates all blocks and edges linearly.

6. Numerical results

The results are presented based on structural displacements, swiveling frequencies, number of coupling steps, robustness of the mesh movement methods and their computational effort. First, small deformations are considered

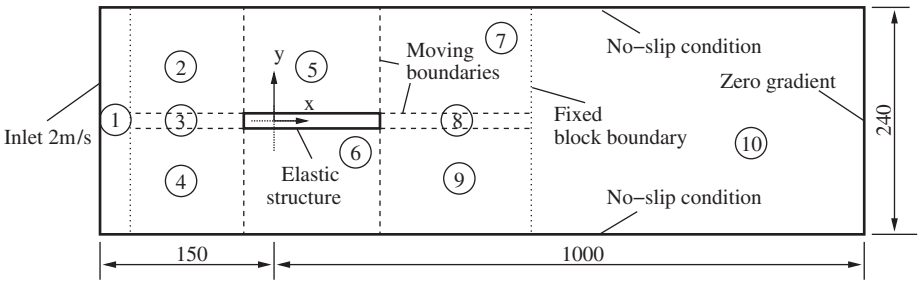

Fig. 5. Geometric properties (in mm) and formation of structured blocks.

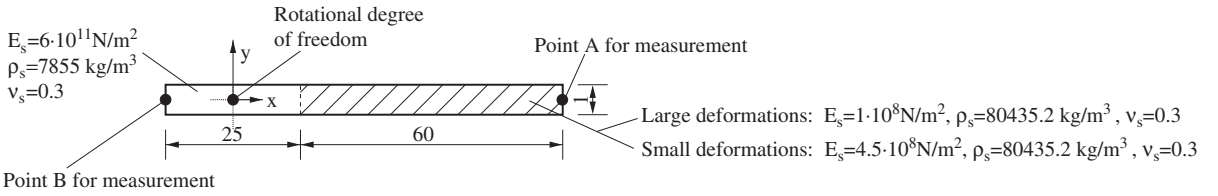

Fig. 6. Structural properties.

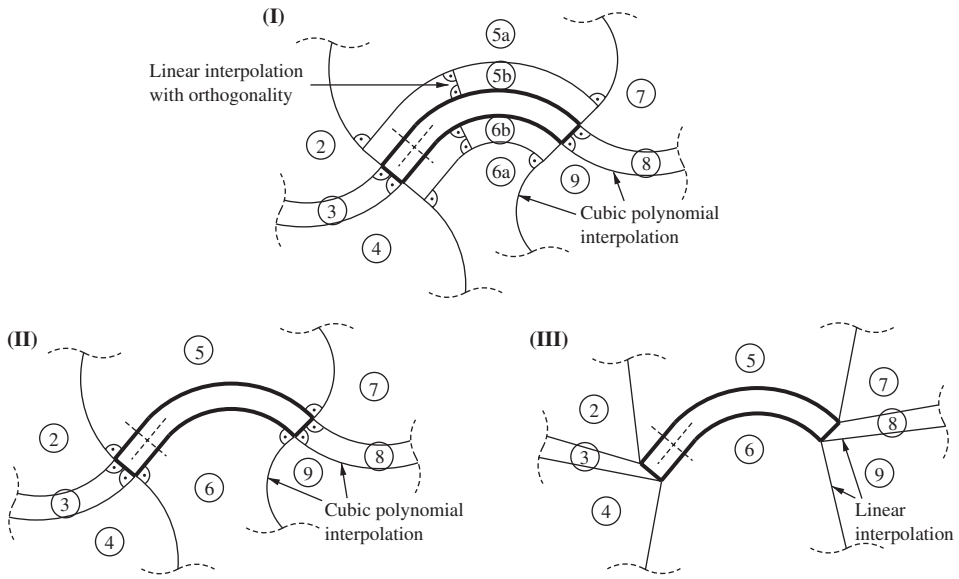

Fig. 7. Boundary discretizations for reference solution (I), elliptic, elliptic-orthogonal, TFI (II) and linear interpolation (III).

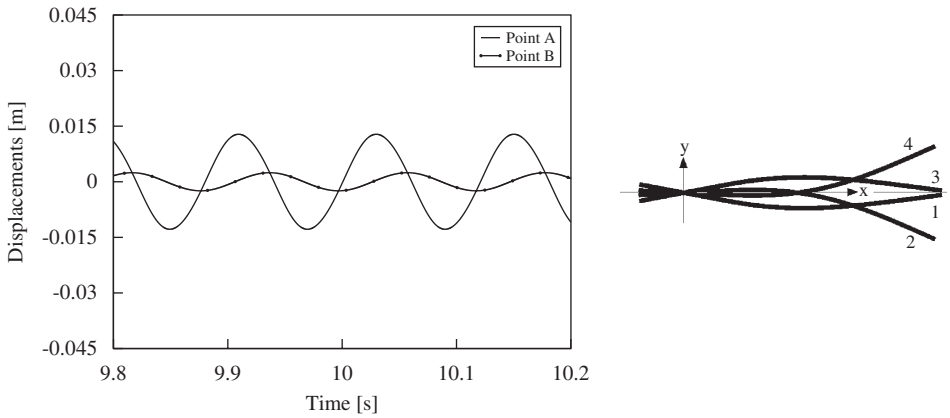

Fig. 8. Structural small displacements (left) and overall deformations (right).

achieved with high Young's modulus for the rear part, see Fig. 6, afterwards, a case with smaller Young's modulus and large deformations is studied.

6.1. Small deformations

Fig. 8 (left) shows the temporal development of structural displacements of front and rear points (A, B). The oscillations are non-linear with constant amplitudes. Fig. 8 (right) illustrates the overall deflection. The motion during one period is represented, e.g., by four numbered superimposed deformations.

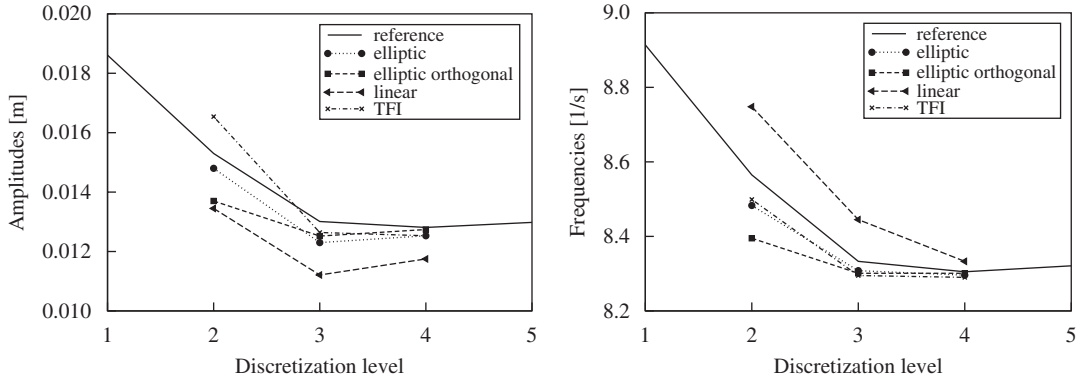

Fig. 9. Amplitudes of rear Point A (left) and swiveling frequencies (right), small deformations.

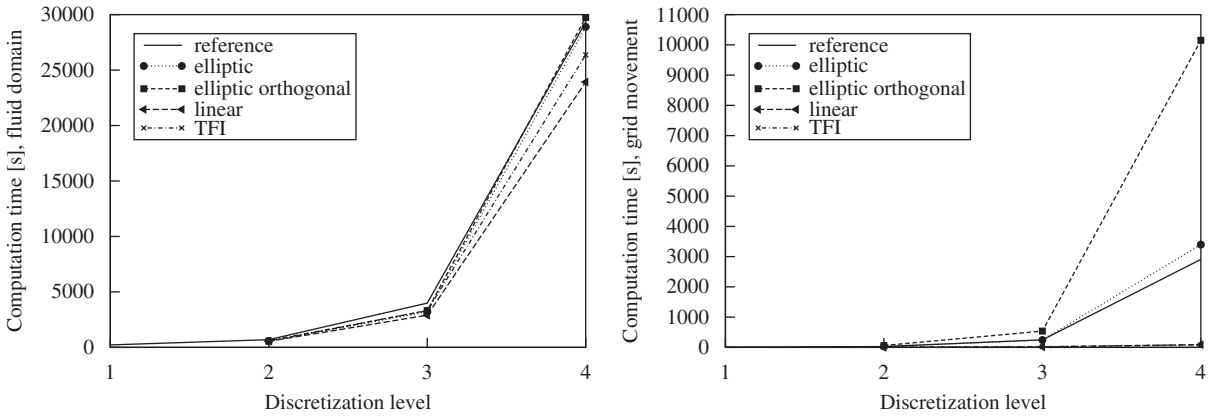

Fig. 10. Computation times for the fluid domain (left) and grid movement (right), small deformations.

In Fig. 9 (left) the amplitudes of the rear point A is shown when using the different mesh moving techniques and different grid levels. The reference values are obtained with the mixed method. The corresponding values for grid level 5 are assumed to be the most accurate ones. This method reproduces a swiveling motion even for the coarsest mesh. The best result is achieved with the orthogonal method followed closely by the elliptic and the TFI. The linear interpolation produces most deviations. The same statement is valid for the swiveling frequencies, shown in Fig. 9 (right).

Fig. 10 (left) compares the computation times for the flow solver for one period (the computation times for the structural part and the data exchange are for all movement techniques nearly the same and are negligibly small. Thus, the overall computation time is the sum of flow solver time and grid movement time). As can be seen, the elliptic approaches are similar, the TFI and linear interpolation are a little faster. Fig. 10 illustrates the computation times for the grid movement procedure. Up to discretization level 3 all methods remain reasonably efficient but then computation times for the orthogonal approach increase dramatically. The other elliptic methods also lead to more computational effort. However, the algebraic methods require negligible grid generation times.

Table 1 shows the average number of coupling iterations for one period. It can be stated that the amount of coupling steps is largely independent of the grid size and the grid movement technique.

6.2. Large deformations

Now, large deformations are considered obtained with a small Young's modulus for the membrane rear part (see Fig. 6). In Fig. 11 displacements of point A and the corresponding superimposed deformations are presented. During the motion the structure occupies, for example, the four numbered stages. A comparison with Fig. 8 illustrates the taller

Table 1
Number of FSI-iterations per period (59 time steps) for small deformations

Discretization level	Mixed reference	Elliptic		Algebraic	
		Non-orthogonal	Orthogonal	TFI	Linear
1	931	–	–	–	–
2	970	1003	1015	977	873
3	944	986	1108	960	864
4	961	1013	2004	973	892
5	949	–	–	–	–

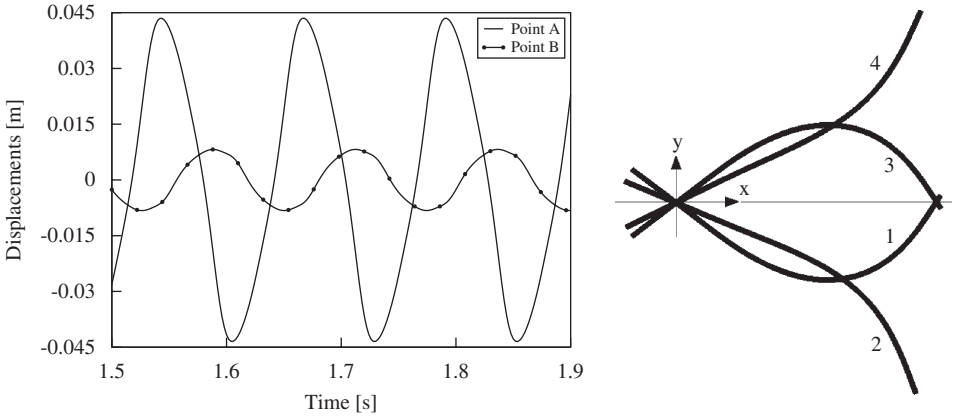

Fig. 11. Structural large displacements (left) and overall deformations (right).

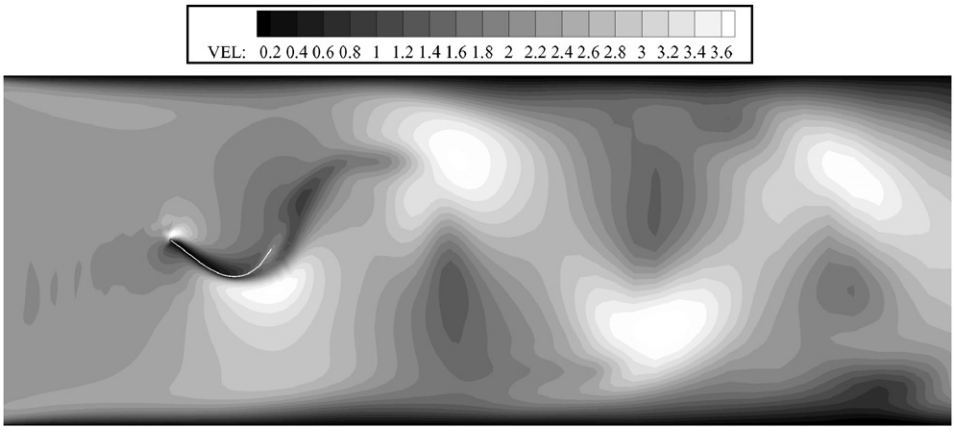

Fig. 12. Velocity field (m/s) for large structural oscillations.

amplitudes and deflections. Fig. 12 shows the velocity field with the structure in a stage corresponding to state 1 in Fig. 11 (right).

Fig. 13 (left) shows the amplitudes for different grids obtained with the various grid movement methods. The linear interpolation works up to discretization level 3; however, stronger refinement increases the amplitudes and grid folding occurs. The TFI leads to completely distorted meshes for all grids. The elliptic approaches give nearly identical results. The same is valid for the swiveling frequencies which are shown in Fig. 13 (right).

Fig. 14 compares computation times for the flow solver for one period (the computation times for the structural part and the data exchange are for all movement techniques nearly the same and are negligibly small. Thus, the overall

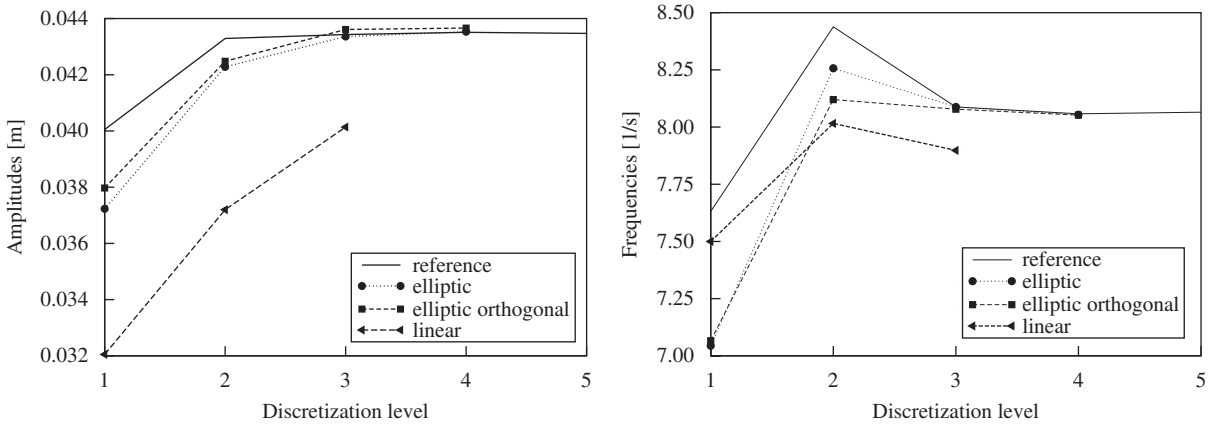

Fig. 13. Amplitudes of rear Point A (left) and swiveling frequencies (right), large deformations.

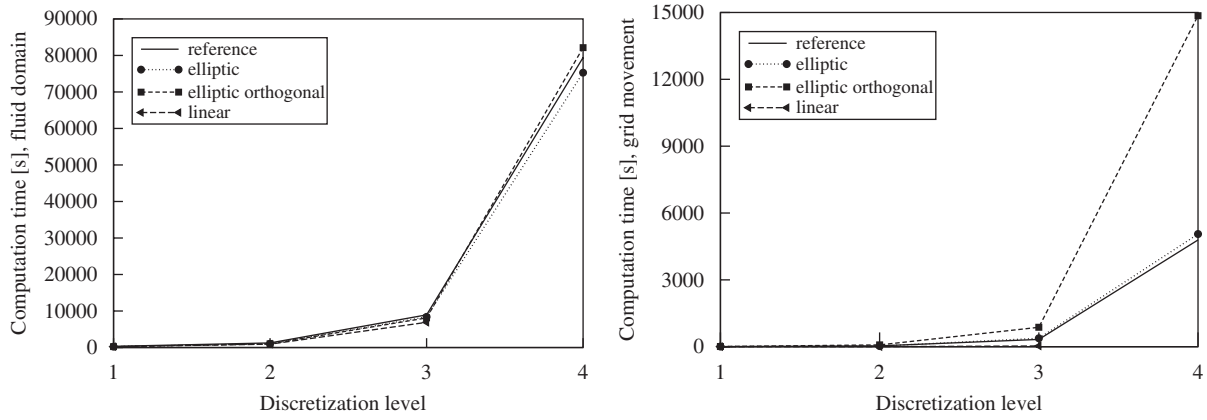

Fig. 14. Computation times for the fluid domain (left) and grid movement (right), large deformations.

Table 2
Number of FSI-iterations per period (62 time steps) for large deformations

Discretization level	Mixed reference	Elliptic		Algebraic	
		Non-orthogonal	Orthogonal	TFI	Linear
1	1101	1084	1092	Grid folding	984
2	1129	1118	1149	g.f.	1028
3	1119	1122	1406	g.f.	1034
4	1130	1129	3089	g.f.	g.f.
5	1158	–	–	–	–

computation time is the sum of flow solver time and grid movement time). All elliptic approaches require nearly the same computational effort for the solution on the finest discretization level. Taking additionally the grid movement procedure into account, see Fig. 14 (right), the orthogonal method is considerably more time consuming than the other elliptic methods.

Table 2 shows the average number of coupling iterations for one period. Comparing Tables 2 and 1, one can state that the behaviour of coupling steps is the same for large and small deformations, i.e., mostly independent of refinement levels and mesh movement methods.

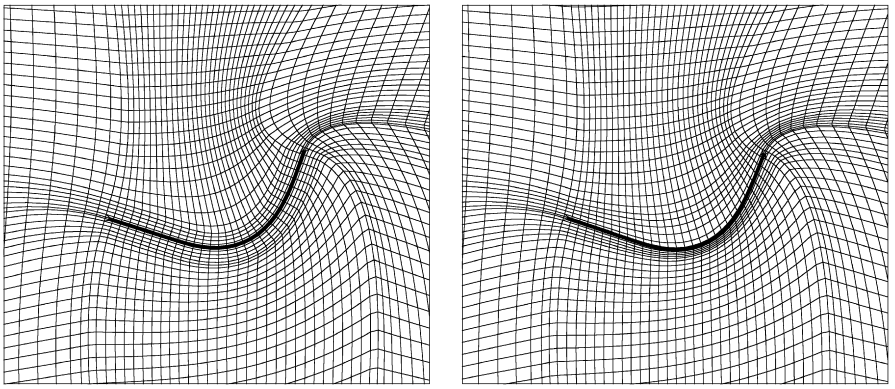

Fig. 15. Mesh deformations for the mixed method (left) and pure elliptic method (right) for large structural deflection.

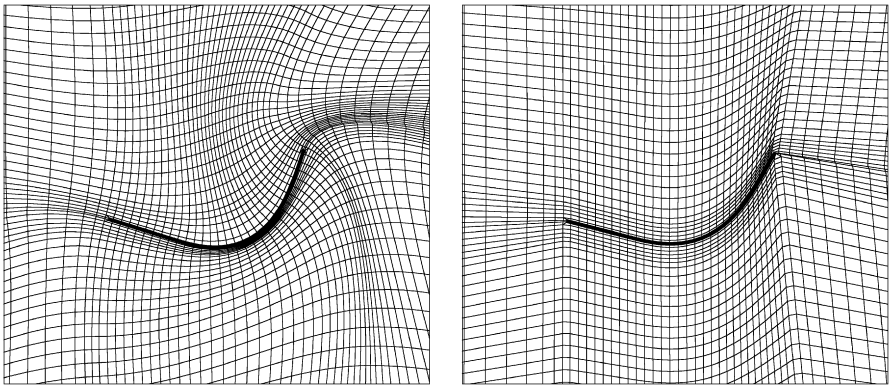

Fig. 16. Mesh deformations for elliptic-orthogonal method (left) and linear interpolation (right) for large structural deflection.

Fig. 15 shows the moved meshes (discretization level 3) around the structure at a point of large deflection for the mixed and the pure elliptic methods. It illustrates the good discretization near boundary regions for the mixed method which is the reason for the good results. This approach combining elliptic and algebraic methods even succeeded for very huge deformations; however, grid folding may occur near the boundary for locally huge rotations. Employing the pure elliptic method for all domains, one can recognize the shrunk and stretched grid lines near the structure. Recall from the previous results that this grid spacing variation hardly influences the accuracy. Note that providing sufficient refinement, grid folding is impossible with this smoothing technique. Fig. 16 (left) demonstrates the exact orthogonalization on all boundaries for the elliptic-orthogonal method leading to a very smooth mesh. Comparing with the pure elliptic method the variation of grid spacing near boundary regions is more distinct. The poor accuracy of the linear interpolation becomes obvious from Fig. 16 (right). The grid lines at the structural rear part are nearly tangents. Taller amplitudes obviously will cause grid folding. Since the TFI leads to extremely distorted meshes the corresponding grid is omitted.

7. Conclusion

Mesh movement techniques for block-structured grids and their influence on laminar fluid–structure interaction computations have been studied. The investigations have been performed on four successive refined grids for small and large structural deformations. We considered algebraic, elliptic and mixed approaches.

In case of small deformations the orthogonal method is disadvantageous due to huge grid computation times. The linear interpolation is also not advisable because of the poor accuracy. Since the TFI provides a similar accuracy as the elliptic methods, but is much faster, it is the favourable technique for block-structured moving meshes undergoing small deformations.

In case of large deformations both algebraic methods failed due to grid folding. The orthogonal approach is not advisable because of enormous grid computation times. The pure elliptic and the mixed method are recommended. They are equally time consuming and provide the same accuracy.

For all mentioned grid movement techniques, the algebraic methods [see Thompson et al. (1999)], the pure elliptic grid generation [see Spekreijse (1995)] and the mixed approach, can also be applied for three-dimensional (3-D) domains, except the orthogonal method. In future work corresponding investigations will be extended to 3-D cases. Up to now, the transfinite and the linear interpolations have been implemented into the employed 3-D flow solver. They show similar behaviour compared to the 2-D case.

Acknowledgement

The financial support of the work by the *Deutsche Forschungsgemeinschaft* within the Research Unit 493 *Fluid–Structure Interaction*: *Modelling*, *Simulation*, *Optimization* is gratefully acknowledged.

References

Albert, M.R., O'Neill, K., 1986. Moving boundary-moving mesh analysis of phase change using finite elements with transfinite mappings. International Journal for Numerical Methods in Engineering 23, 591–607.

Baker, T.J., 2001. Mesh deformation and reconstruction for time evolving domains. AIAA Paper 2001-2535.

Bar-Yoseph, P.Z., Mereu, S., Chippada, S., Kalro, V.J., 2001. Automatic monitoring of element shape quality in 2-D and 3-D computational mesh dynamics. Computational Mechanics 27, 378–395.

Demirdžić, I., Perić, M., 1988. Space conservation law in finite volume calculations of fluid flow. International Journal for Numerical Methods in Fluids 8, 1037–1050.

Donea, J., Huerta, A., Ponthot, J.-Ph., Rodríguez-Ferran, A., 2004. Arbitrary Lagrangian–Eulerian methods. Encyclopedia of Computational Mechanics 1, 14.

Farhat, C., Degand, C., Koobus, B., Lesoinne, M., 1998. Torsional springs for two-dimensional dynamic unstructured fluid meshes. Computer Methods in Applied Mechanics and Engineering 163, 231–245.

Fraunhofer, SCAI, 2004. MpCCI—mesh-based parallel code coupling interface. User Guide V2.0.

Löhner, R., Yang, C., 1996. Improved ALE mesh velocities for moving bodies. Communications in Numerical Methods in Engineering 12, 599–608.

Longatte, E., Bendjeddou, Z., Souli, M., 2003. Application of arbitrary Lagrange Euler formulations to flow-induced vibration problems. Journal of Pressure Vessel Technology 125, 411–417.

Murayama, M., Nakahashi, K., Matsushima, K., 2002. Unstructured dynamic mesh for large movement and deformation. AIAA Paper 2002-0122

Ogden, R.W., 1997. Non-Linear Elastic Deformations. Dover Publications, New York.

Schäfer, M., Meynen, S., Sieber, R., Teschauer, I., 2001. Efficiency of multigrid methods for the numerical simulation of coupled fluid–solid problems. In: Scientific Computing and Applications, Advances in Computation: Theory and Practice. Nova Science Publishers, Huntington, pp. 257–266.

Schäfer, M., Heck, M., Yigit, S., 2006. An implicit partitioned method for numerical simulation of fluid–structure interaction. In: Lecture Notes in Computational Science and Engineering, vol. 53. Springer, Berlin.

Spekreijse, S.P., 1995. Elliptic grid generation based on Laplace equations and algebraic transformations. Journal of Computational Physics 118, 38–61.

Stein, K., Tezduyar, T., Benney, R., 2003. Mesh moving techniques for fluid–structure interactions with large displacements. Journal of Applied Mechanics 70, 58–63.

Taylor, R.L., 2002. FEAP, A Finite Element Analysis Program. Version 7.4 User Manual. University of California, Berkeley.

Taylor, R.L., 2003. FEAP, A Finite Element Analysis Program. Version 7.5 Theory Manual. University of California, Berkeley.

Thompson, J.F., Soni, B.K., Weatherill, N.P., 1999. Handbook of Grid Generation. CRC Press LLC, Boca Raton, FL.

Truesdell, C., Noll, W., 2004. The Non-Linear Field Theories of Mechanics, third ed. Springer, Berlin.

Yang, Z., Mavriplis, D.J., 2005. Unstructured dynamic meshes with higher-order time integration schemes for the unsteady Navier–Stokes equations. AIAA Paper 2005-1222